

Extreme Events Prediction from Nonlocal Partial Information in a Spatiotemporally Chaotic Microcavity Laser

V. A. Pammi,¹ M. G. Clerc², S. Coulibaly³, and S. Barbay¹

¹*Université Paris-Saclay, CNRS, Centre de Nanosciences et de Nanotechnologies, 91120 Palaiseau, France*

²*Departamento de Física and Millenium Institute for Research in Optics, Facultad de Ciencias Físicas y Matemáticas, Universidad de Chile, Casilla 487-3, Santiago, Chile*

³*Univ. Lille, CNRS, UMR 8523—PhLAM—Physique des Lasers Atomes et Molécules, F-59000 Lille, France*

 (Received 26 August 2022; revised 22 December 2022; accepted 27 March 2023; published 31 May 2023)

The forecasting of high-dimensional, spatiotemporal nonlinear systems has made tremendous progress with the advent of model-free machine learning techniques. However, in real systems it is not always possible to have all the information needed; only partial information is available for learning and forecasting. This can be due to insufficient temporal or spatial samplings, to inaccessible variables, or to noisy training data. Here, we show that it is nevertheless possible to forecast extreme event occurrences in incomplete experimental recordings from a spatiotemporally chaotic microcavity laser using reservoir computing. Selecting regions of maximum transfer entropy, we show that it is possible to get higher forecasting accuracy using nonlocal data vs local data, thus allowing greater warning times of at least twice the time horizon predicted from the nonlinear local Lyapunov exponent.

DOI: [10.1103/PhysRevLett.130.223801](https://doi.org/10.1103/PhysRevLett.130.223801)

The prediction of extreme event (EE) occurrences, while having potentially a large impact in many fields of science and everyday life, remains a challenge, especially in large and complex spatiotemporal systems [1–9]. EEs, which are rare and intense amplitude phenomena—as compared to the long-time average of an observable in a given system [10]—have been found in many types of systems [11], either natural or in laboratory experiments. In the latter case, optical systems have played a great role because of the analogy between oceanic rogue waves and optical pulse propagation in nonlinear optical fibers [12,13], allowing one to generate and study these EEs with a large statistics and in a controlled environment. EEs have also been found in nonlinear optical dissipative systems displaying chaos [14–18] or spatiotemporal chaos [19–21]. Likewise, model-free prediction of low- [22–25] and high-dimensional [26–28] chaotic time series have been made possible thanks to the advent of machine learning techniques. However, they usually require the precise knowledge of the whole spatiotemporal history of a dynamical field, which is often impossible in real situations where only a part of the dynamics is observable while some dynamical variables remain hidden and cannot be recorded. When a dynamical variable is observed and used to predict the outcome of another variable, the concept of cross-prediction has been introduced and tested [29,30]. The application of model-free techniques is more challenging when dealing with experimental and natural data [31], where the resolution of the measurements in time and space is limited. Recent results have been obtained in this area for the prediction of rogue solitons in supercontinuum generation in an optical

fiber [32,33] and the space-time localization of extreme wind speeds in the North Atlantic ocean [8]. In Ref. [33], the system is purely temporal and a spatiotemporal map is obtained by a pseudo-space reconstruction. Precursors identified in a different location of the reconstructed pseudo-space therefore belong to the past of the system's evolution, not to a genuine different spatial location. In Ref. [8], the full spatiotemporal field is recorded and used for the forecast, thanks to the relatively slow timescale of the system's evolution.

In this Letter, we use a model-free reservoir computing approach for the prediction of EE occurrences with experimental data from a spatiotemporal chaotic broad-area laser [20], where only partial information of the past spatiotemporal field is known. The only accessible observable is the laser intensity (not the laser material dynamics), and the dynamics can only be known accurately and simultaneously at two given locations in space. This simulates the common situation in practice where the spatiotemporal field is only scarcely sampled in space. We identify the spatial locations of potential precursors using an information theoretic measure, namely transfer entropy [34]. In contrast to Ref. [33], where the precursors have a size of the same order of magnitude as the one of the extreme pulses, here the precursors cannot be identified reliably but are mostly hidden in the system's dynamical fluctuations and in the detection noise. A classification task is performed using reservoir computing to identify EEs in advance, using local and nonlocal information. We compare the prediction results and identify regimes where the nonlocal, cross-prediction task yields better prediction accuracy than the local task.

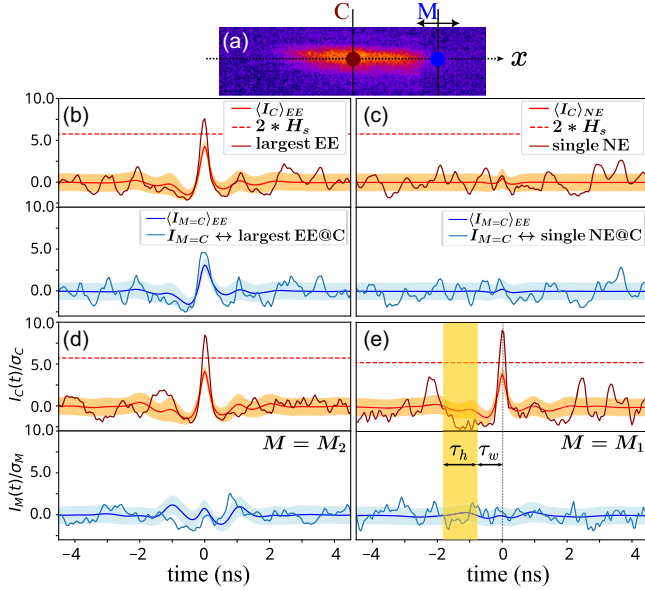


FIG. 1. (a) Microcavity near-field image above lasing threshold. (b)–(e) Simultaneous recording of scaled intensities at C (fixed photodetector, upper) and M (mobile photodetector, lower) for specific events at C (placed at $t = 0$): an EE is present (b), (d), (e) or not present (c) at C . The photodetector is located at $x_M = 0 \mu\text{m}$ in (b), $x_{M_2} = +12.3 \mu\text{m}$ in (d), and $x_{M_1} = -13.8 \mu\text{m}$ in (e). Red and black lines: average timetraces over the ensemble of EE or NE and associated standard deviations (orange and light blue shaded areas). Dark red: largest EE’s timetrace, in (b), (d), (e) [respectively, single random NE in (c)] recorded at C with the simultaneous timetrace recorded at M (light blue). Red dashed line: EE threshold $2 \times H_s$ (to be compared to the pulse height H from the trough to peak, not to the peak value). Yellow shaded area in (e): information used for the prediction of an event at $t = 0$, with history time τ_h and warning time τ_w .

We investigate a quasi-1D broad-area microcavity laser with integrated saturable absorber, which has been shown, both experimentally and numerically, to display spatiotemporal chaos and EEs [20,35]. The observed spatiotemporal chaos results from a chaotic alternation of amplitude and phase turbulence phenomena [36]. The microcavity laser pumped area is delimited by a clear aperture of $10 \times 80 \mu\text{m}^2$ and emits at $\lambda_c \simeq 980 \text{ nm}$. Transverse spatial coupling in the microresonator is obtained through light diffraction with a diffraction length $w_d \simeq 7.4 \mu\text{m}$ [20]. The detailed optical setup is described in Ref. [20] and recalled in the Supplemental Material (SM) for completeness. This system has the advantage of having fast timescales, on the order of hundreds of picoseconds, thus facilitating the sampling of a large number of low probability events in a single experimental run. EEs are qualified using the standard definitions used in hydrodynamics, where these phenomena are coined “rogue waves” [11].

The dynamics recorded at the center of the laser [see Fig. 1(a)] displays large amplitude fluctuations [Figs. 1(b), 1(d), and 1(e)]. These fluctuations of height H (defined as

the maximum between the amplitudes measured at the left and right sides of the pulse) can be classified into two classes: extreme events (EE) or nonextreme events (NE). The classification criteria for EEs is $H \geq 2H_s$, where H_s , the significant height, is simply the average of the height of the events in the highest tercile. For technical reasons, it is not possible to access the evolution of the whole section of the laser with the required detection bandwidth. Only partial information is available—namely, we detect the simultaneous evolution in two different points, one fixed located at the center of the laser $I_C(t) = I(x_C, t)$, and one mobile across the transverse section $I_M(t) = I(x_M, t)$. In Fig. 1(b), the intensity of EEs simultaneously measured by the two photodetectors at the same location displays correlated timetraces. The average time trace of EEs shows some oscillations around the peak value at $time = 0$ that quickly dampen away from it, evidencing a typical temporal pattern for EEs. In Fig. 1(c) by comparison, NEs are completely uncorrelated, which results in a very flat average time trace. Away from the correlation width of an EE, at M_1 , an EE recorded in C is accompanied by no clear sign in the time trace at M_2 , which displays a dynamics very similar to the one recorded for a NE in Fig. 1(c). By contrast, the average signal recorded at $M = M_2$ [Fig. 1(d)] shows a small fluctuation for $-1.5 \leq t \leq -0.5 \text{ ns}$ that may point to the presence of a precursor. However, the precursor identification is rendered difficult since the signal fluctuations are large and on the same order of magnitude as the signal itself, as can be seen on the nonaveraged timetrace. The identification of potential precursors can be made easier using the tool of transfer entropy described below.

The dynamical complexity of the dataset can be estimated from the Lyapunov spectra computed for the individual local recordings $I_M(t)$. From these, the largest Lyapunov exponent λ_M can be extracted, giving access to a global, mean maximum prediction time $\tau_p \simeq (1/\lambda_M) \ln(\Delta/\delta_0)$ [37,38], with δ_0 the initial perturbation and Δ the resolution of the measurement. The mean Kaplan-Yorke dimension D_{KY} and fractal dimension D_f of the attractor are, respectively, $\langle D_{KY} \rangle \simeq 11$ and $\langle D_f \rangle \simeq 7.1$ [Fig. 2(a)], which are consistent with a high-dimensional chaos. A more precise estimate of the prediction time horizon is given using the rate of growth of initial error rate Φ computed in Fig. 2, which can be extracted from the nonlinear local Lyapunov exponent [38] (see SM [39]). The prediction horizon time can be defined as the time at which $\log(\Phi)$ reaches 90% of its saturation value and is of the order of 0.47 ns here. Using side results (see SM), we can also estimate $\delta_0 \simeq 3 \times 10^{-4}$ and, assuming $\Delta \simeq 5 \times 10^{-3}$, which corresponds to a SNR of 1, and extracting the mean maximum Lyapunov exponent from Fig. 2 ($\lambda_M = 7.6 \text{ ns}^{-1}$), we get a mean maximum prediction time $\tau_p = 0.37 \text{ ns}$. This time is slightly smaller than the time obtained from $\log(\Phi)$, as expected, but is still larger than the Lyapunov time usually considered as a time horizon indicator $\tau_L = \langle \lambda_M \rangle^{-1} = 0.13 \text{ ns}$. Recent results showed that machine

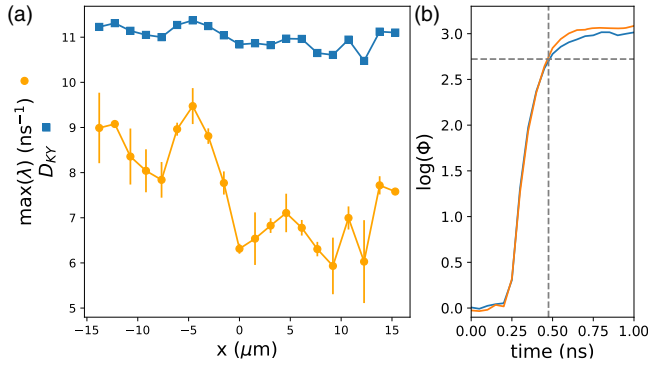


FIG. 2. (a) Largest Lyapunov exponent $\lambda_M = \max(\lambda)$ and Kaplan-Yorke dimension D_{KY} of the timetraces versus recording position. (b) Initial error growth rate for the laser intensity versus time computed at C for both photodetector recordings. The extracted prediction time horizon (see text) is 0.47 ns.

learning aided model-free predictions of high-dimensional chaotic systems was possible up to about 6 Lyapunov times [26,29,47–49].

Early warning signs of EEs, also called precursors, have been considered in many previous works (e.g., in [1,6,50]), including in low-dimensional optical systems [51–54]. To identify potential regions of precursors, we consider transfer entropy [34], similarly as in [33], which measures the information transfer between two signals. It is more robust than, e.g., a simple cross-correlation since it uses conditional probabilities instead of correlations.

We introduce the two-dimensional effective transfer entropy $T_{M \rightarrow C}^{\text{eff}}(x_M, \tau_w)$ (see SM [39]), which measures the information gained at point C (in bits) from the knowledge of a history of duration τ_h in the past at M [see Fig. 1(e)], with τ_w parameterizing the time delay in the past. It is obtained by subtracting to the transfer entropy $T_{M \rightarrow C}$ the transfer entropy for surrogate data in M , allowing comparison between transfer entropies computed using different τ_h . $T_{M \rightarrow C}^{\text{eff}}(x_M, \tau_w)$ is calculated and plotted in Fig. 3(a) for a history of size $\tau_h = 0.050$ ns. It displays three regions of interest. A large central lobe centered around $x_M \simeq x_C$, which corresponds to causal information in the immediate spatiotemporal surrounding of the EE, and two disconnected regions almost symmetric about the temporal axis, which we identify as the location of potential precursors (around P_1 and P_2). It is clearly seen that EEs extend over a finite length of $10 \mu\text{m}$ width, as already noted in Ref. [20]. At lags around $\tau_w = 5\Delta t = 0.25$ ns, there is a net transfer of information to the center of the laser at $\tau_w = 0$. This corresponds to the immediate warning signal of the EE formation. More importantly, there are disconnected regions around P_1 and P_2 at delay times $\tau_w \simeq 0.9$ ns where there is a net positive transfer of information outside of the initial correlation length of the system. In the following, we are going to use this knowledge for a

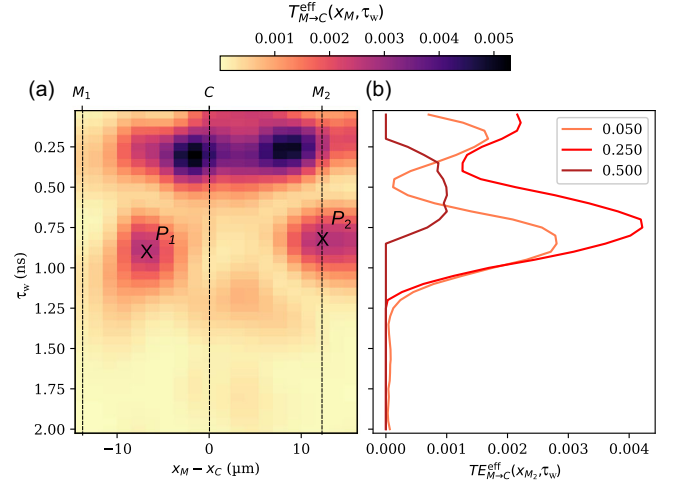


FIG. 3. Effective transfer entropy $T_{M \rightarrow C}^{\text{eff}}$ as a function of x_M and delay τ_w for $\tau_h = 1$, $\Delta t = 0.050$ ns and (b) at M_2 for $\tau_h = 0.050$, 0.250, 0.500 ns. P_1 and P_2 locate the main precursor regions in the spatiotemporal diagram. $T_{M \rightarrow C}^{\text{eff}}$ is smoothed by a small Gaussian kernel (see SM for the original data).

model-free prediction of the occurrence of EEs given the past dynamical information.

A dataset is built after identifying events times t_E of intensity maxima at C and recording the signal at M for a duration τ_h corresponding to m samples, i.e., from $[t_E - \tau_w - \tau_h, t_E - \tau_w]$, τ_w being the warning time [see Fig. 1(e)]. Events at C are labeled as EE or NE. Since EEs are rare by definition, a balanced dataset is built by retaining all the N EEs and choosing an equal number of NEs at random. This allows us to use a standard metric for the loss function [7]. The dataset therefore consists of $2 \times N$ timetraces associated to labels that identify their categories, 70% of which is used as training data and 30% as testing data. The prediction task is carried out using reservoir computing (RC). RC has been used for prediction on various low- and high-dimensional dynamical systems [24,26,55–57]. It is particularly interesting as reservoirs are themselves dynamical systems, making them ideal candidates to map other dynamical systems. While we have tested other machine learning algorithms (K-nearest neighbors, long-short term memory, logistic regression), none of them showed a significant superiority and RC happened to be the one with the overall best performance [58]. The reservoir generation and update follow the standard procedure detailed in the SM. It comprises $N = 50$ nodes each with a hyperbolic tangent activation function and is initialized by a null state. Its parameters were optimized thanks to a hyperoptimization routine. At the end of the input sequence, the state of the reservoir nodes is stored forming an output vector of length N . Thus, an input time series of m samples is converted into a vector of at most N values, which is a representation of the input data. A logistic classifier assigning a class EE or NE is then trained on all the training time sequences. The forecasting accuracy

of an EE at C for a history $\tau_h = 1.75$ ns versus the warning time τ_w is shown in Fig. 4(a). It is displayed for different training data: using the local information at C , or the nonlocal data at M_1 or M_2 . Note that the accuracy does not depend significantly on the history length after a certain length is reached (see SM). In the first case, an accuracy close to 1 is obtained for small warning times, since this forecasting task is linear and simple. As τ_w increases, the forecasting accuracy also decreases almost monotonically towards 0.5, i.e., to the absence of forecasting power. The same behavior occurs using nonlocal training data, though with important differences between M_1 and M_2 . At M_1 , the forecasting accuracy is always low since there is almost no information present at this location, as can be checked in Fig. 3. The forecasting accuracy using nonlocal data at M_2 , on the contrary, is close to 0.8 for small warning times and decreases steadily until about 1.2 ns where the accuracy drops considerably and is on par with the one computed using data at M_1 . However, most interestingly, there is a window of forecasting where it is possible to obtain slightly higher accuracy with the nonlocal data at M_2 rather than using the local data at C . This illustrates the importance of analyzing the transfer entropy pattern in Fig. 3(a), which can allow one to improve the prediction accuracy by evidencing the spatiotemporal location of potential precursors. The forecasting accuracy at M_2 drops at $\tau_w \simeq 1$, which is more than twice the time horizon inferred previously and also about 7.5 times larger than the Lyapunov time. This corresponds also to the time at which the logistic regression alone gives comparable results with the RC approach. It also relates to the drop observed for the effective transfer entropy computed in Fig. 3(b) for different warning times. This means that no useful further information can be extracted from the input time series past this timescale. For smaller warning times, the reservoir is able to improve slightly the forecasting accuracy with respect to a simpler logistic regression approach. By contrast when $\tau_w \gg 1$, very little information can be extracted for the prediction as evidenced the low transfer entropy computed.

In Figs. 4(b) and 4(c), we analyze how our model-free approach classifies EEs depending on their actual heights. As shown on the testing dataset histogram of heights [Fig. 4(b)], despite the fact that the training sets have been balanced, large EEs are still far less frequent than smaller ones and will therefore participate less to the training. The probability $P(\text{Event} = \text{EE}|H)$ of forecasting as an EE an event of actual height H at C , given the knowledge of a history of nonlocal data at M_2 characterized with $\tau_w = 1$ ns and $\tau_h = 1.75$ ns, is shown in Fig. 4(c). In the perfect case, the probability would evaluate to 1 above $2H_s$ and zero below. It increases with H and generally reaches 1 for the largest EE heights' values, while the complementary probability $P(\text{Event} = \text{NE}|H)$ goes to zero (green and yellow histograms, respectively). This trend is true for the results shown in Figs. 4(b) and 4(c), obtained for two

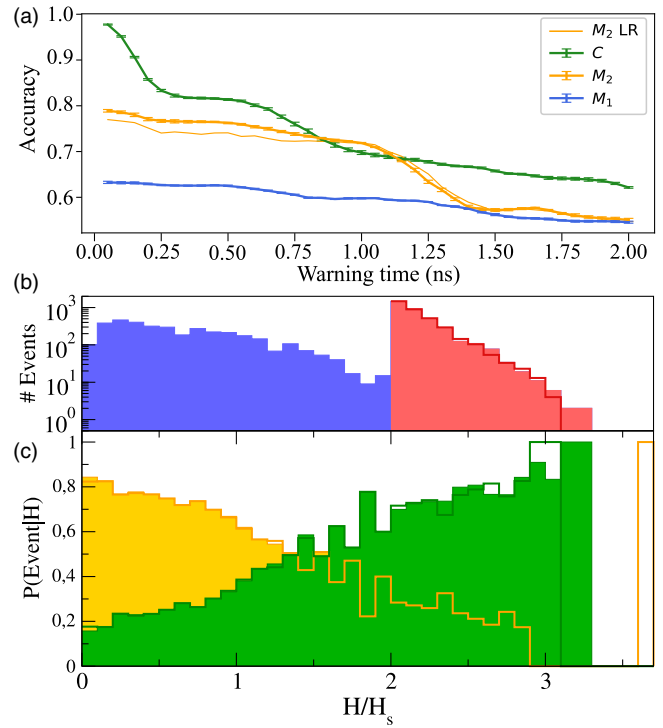


FIG. 4. (a) Mean EE forecasting accuracy at C with $\tau_h = 1.75$ ns versus the warning time τ_w , using either local (at C) or nonlocal (at M_1 or M_2) data as input. The mean and standard deviation are computed with 10 different realizations of the reservoir. Thin line: nonlocal forecasting at M_2 using logistic regression alone. (b) Histogram of the testing dataset heights' distribution (blue, NE; red, EE events). (c) Classification probability as an EE (green) or a NE (complementary, orange) of an event of actual height H occurring $\tau_w = 1$ ns in the future at C from the knowledge of a history of $\tau_h = 1.75$ ns duration of the nonlocal data at M_2 . Two different realizations of the testing dataset are illustrated (plain and empty histograms).

different training sets, and shows that while large EEs are less frequent in the training dataset, their prediction accuracy increases with their height, resulting in a usually very good prediction for the largest EEs. We note, however, that some statistical fluctuations can remain in the forecasting results, as can be seen on the far right of Fig. 4(c), where an isolated event has been misclassified in one realization of the train and test datasets' partitions.

In conclusion, we have shown that a model-free approach based on reservoir computing can successfully classify, with a reasonable accuracy, the occurrence of EEs in a dataset of an experimental system displaying high-dimensional spatiotemporal chaos from the partial knowledge of the history of the spatiotemporal field. Using the transfer entropy concept, we identify specific spatiotemporal regions with high information flow pointing to potential precursors, which in our specific case are hidden in the dynamical fluctuations or detection noise. We find that while the prediction using the local information gives generally the best accuracy, forecasting from the nonlocal precursor region can yield

comparable to slightly higher accuracy in a window of large warning times. The forecasting ability extends to at least twice the time horizon computed from the nonlinear local Lyapunov exponent of the system and about 7.5 times the Lyapunov time before dropping to a random prediction. We believe these results pave the way to extreme forecasting in other areas of science, with applications to many natural systems, including in geoscience for the detection of earthquakes where the precursors are unknown and the spatial detection is incomplete.

M. G. C. acknowledges the financial support of ANID-Millennium Science Initiative Program-ICN17_012 (MIRO) and FONDECYT Project No. 1210353. This work was partially supported by the French Renatech network.

-
- [1] N. Akhmediev, A. Ankiewicz, J. Soto-Crespo, and J. M. Dudley, *Phys. Lett. A* **375**, 541 (2011).
- [2] A. L. Latifah and E. van Groesen, *Nonlinear Processes Geophys.* **19**, 199 (2012).
- [3] M.-R. Alam, *Geophys. Res. Lett.* **41**, 8477 (2014).
- [4] S. Birkholz, C. Brée, A. Demircan, and G. Steinmeyer, *Phys. Rev. Lett.* **114**, 213901 (2015).
- [5] M. Erkintalo, *Nat. Photonics* **9**, 560 (2015).
- [6] C. Bayındır, *Phys. Lett. A* **380**, 156 (2016).
- [7] S. Guth and T. P. Sapsis, *Entropy* **21**, 925 (2019).
- [8] J. Jiang, Z.-G. Huang, C. Grebogi, and Y.-C. Lai, *Phys. Rev. Res.* **4**, 023028 (2022).
- [9] P. R. Vlachas, G. Arampatzis, C. Uhler, and P. Koumoutsakos, *Nat. Mach. Intell.* **4**, 359 (2022).
- [10] G. Nicolis and C. Nicolis, *Foundations of Complex Systems: Emergence, Information and Prediction*, 2nd ed. (World Scientific, Singapore, 2012).
- [11] M. Onorato, S. Residori, U. Bortolozzo, A. Montina, and F. Arecchi, *Phys. Rep.* **528**, 47 (2013).
- [12] D. R. Solli, C. Ropers, P. Koonath, and B. Jalali, *Nature (London)* **450**, 1054 (2007).
- [13] B. Kibler, J. Fatome, C. Finot, G. Millot, F. Dias, G. Genty, N. Akhmediev, and J. M. Dudley, *Nat. Phys.* **6**, 790 (2010).
- [14] C. Bonatto, M. Feyereisen, S. Barland, M. Giudici, C. Masoller, Jose R. Rios Leite, and J. R. Tredicce, *Phys. Rev. Lett.* **107**, 053901 (2011).
- [15] M. G. Kovalsky, A. A. Hnilo, and J. R. Tredicce, *Opt. Lett.* **36**, 4449 (2011).
- [16] C. Lecaplain, P. Grelu, J. M. Soto-Crespo, and N. Akhmediev, *Phys. Rev. Lett.* **108**, 233901 (2012).
- [17] A. K. D. Bosco, D. Wolfersberger, and M. Sciamanna, *Opt. Lett.* **38**, 703 (2013).
- [18] C. R. Bonazzola, A. A. Hnilo, M. G. Kovalsky, and J. R. Tredicce, *Phys. Rev. A* **92**, 053816 (2015).
- [19] N. Marsal, V. Caultet, D. Wolfersberger, and M. Sciamanna, *Opt. Lett.* **39**, 3690 (2014).
- [20] F. Selmi, S. Coulibaly, Z. Loghmani, I. Sagnes, G. Beaudoin, M. G. Clerc, and S. Barbay, *Phys. Rev. Lett.* **116**, 013901 (2016).
- [21] M. G. Clerc, G. González-Cortés, and M. Wilson, *Opt. Lett.* **41**, 2711 (2016).
- [22] J. D. Farmer and J. J. Sidorowich, *Phys. Rev. Lett.* **59**, 845 (1987).
- [23] H. D. I. Abarbanel, R. Brown, J. J. Sidorowich, and L. S. Tsimring, *Rev. Mod. Phys.* **65**, 1331 (1993).
- [24] W. Maass, T. Natschläger, and H. Markram, *Neural Comput.* **14**, 2531 (2002).
- [25] P. Amil, M. C. Soriano, and C. Masoller, *Chaos* **29**, 113111 (2019).
- [26] J. Pathak, B. Hunt, M. Girvan, Z. Lu, and E. Ott, *Phys. Rev. Lett.* **120**, 024102 (2018).
- [27] P. R. Vlachas, W. Byeon, Z. Y. Wan, T. P. Sapsis, and P. Koumoutsakos, *Proc. R. Soc. A* **474**, 20170844 (2018).
- [28] K. Nakai and Y. Saiki, *Phys. Rev. E* **98**, 023111 (2018).
- [29] R. S. Zimmermann and U. Parlitz, *Chaos* **28**, 043118 (2018).
- [30] A. Cunillera, M. C. Soriano, and I. Fischer, *Chaos* **29**, 113113 (2019).
- [31] Y.-G. Ham, J.-H. Kim, and J.-J. Luo, *Nature (London)* **573**, 568 (2019).
- [32] L. Salmela, C. Lapre, J. M. Dudley, and G. Genty, *Sci. Rep.* **10**, 9596 (2020).
- [33] S. Coulibaly, F. Bessin, M. G. Clerc, and A. Mussot, *Chaos, Solitons Fractals* **160**, 112199 (2022).
- [34] T. Schreiber, *Phys. Rev. Lett.* **85**, 461 (2000).
- [35] S. Coulibaly, M. G. Clerc, F. Selmi, and S. Barbay, *Phys. Rev. A* **95**, 023816 (2017).
- [36] S. Barbay, S. Coulibaly, and M. Clerc, *Entropy* **20**, 789 (2018).
- [37] H. Kantz and T. Schreiber, *Nonlinear Time Series Analysis* (Cambridge University Press, Cambridge, England, 2003).
- [38] R. Ding and J. Li, *Phys. Lett. A* **364**, 396 (2007).
- [39] See Supplemental Material at <http://link.aps.org/supplemental/10.1103/PhysRevLett.130.223801> for information on the time horizon estimation, precise definition and computation of the effective transfer entropy map, which includes Refs. [40–46].
- [40] P. Grassberger and I. Procaccia, in *The Theory of Chaotic Attractors* (Springer, New York, 2004), pp. 170–189.
- [41] P. Grassberger and I. Procaccia, *Phys. Rev. Lett.* **50**, 346 (1983).
- [42] P. J. Rousseeuw, *J. Am. Stat. Assoc.* **79**, 871 (1984).
- [43] P. Bryant, R. Brown, and H. D. I. Abarbanel, *Phys. Rev. Lett.* **65**, 1523 (1990).
- [44] A. Wolf, J. B. Swift, H. L. Swinney, and J. A. Vastano, *Physica (Amsterdam)* **16D**, 285 (1985).
- [45] J. Li and R. Ding, *Mon. Weather Rev.* **139**, 3265 (2011).
- [46] S. Behrendt, T. Dimpfl, F. J. Peter, and D. J. Zimmermann, *SoftwareX* **10**, 100265 (2019).
- [47] J. Jiang and Y.-C. Lai, *Phys. Rev. Res.* **1**, 033056 (2019).
- [48] H. Fan, J. Jiang, C. Zhang, X. Wang, and Y.-C. Lai, *Phys. Rev. Res.* **2**, 012080 (2020).
- [49] P. Vlachas, J. Pathak, B. Hunt, T. Sapsis, M. Girvan, E. Ott, and P. Koumoutsakos, *Neural Netw.* **126**, 191 (2020).
- [50] W. Cousins, M. Onorato, A. Chabchoub, and T. P. Sapsis, *Phys. Rev. E* **99**, 032201 (2019).
- [51] J. Zamora-Munt, B. Garbin, S. Barland, M. Giudici, Jose R. Rios Leite, C. Masoller, and J. R. Tredicce, *Phys. Rev. A* **87**, 035802 (2013).
- [52] C. Bonatto and A. Endler, *Phys. Rev. E* **96**, 012216 (2017).

- [53] N. M. Alvarez, S. Borkar, and C. Masoller, *Eur. Phys. J. Special Topics* **226**, 1971 (2017).
- [54] C. Bonazzola, A. Hnilo, M. Kovalsky, and J. Tredicce, *Phys. Rev. E* **97**, 032215 (2018).
- [55] H. Jaeger and H. Haas, *Science* **304**, 78 (2004).
- [56] M. Lukoševičius and H. Jaeger, *Comput. Sci. Rev.* **3**, 127 (2009).
- [57] F. M. Bianchi, S. Scardapane, S. Lokse, and R. Janssen, *IEEE Trans. Neural Networks Learn. Syst.* **32**, 2169 (2021).
- [58] V. A. Pammi, Photonic computing with coupled spiking micropillars and extreme event prediction in microcavity lasers, Theses, Université Paris-Saclay, 2021, <https://theses.hal.science/tel-03634754>.